https://doi.org/10.36375/prepare_u.iiche.a383

Theoretical Studies on the Charge Carrier Mobility and Lattice Thermal Conductivity of Rubidium-based Triiodides Using First Principle Calculation

ANUPRIYA NYAYBAN[1], SUBHASIS PANDA[1*], AVIJIT CHOWDHURY[2]

[1]Department of Physics, National Institute of Technology Silchar, Assam, 788010, India
[2]Department of Condensed Matter Physics and Material Sciences, S.N. Bose National Centre for Basic Sciences, JD Block, Sector III, Salt Lake City, Kolkata 700106, India

**Corresponding author's mail id:subhasis@phy.nits.ac.in*

Abstract:

The spectacular hike in the photo conversion efficiency and the light-harvesting ability of Perovskites-based solar cells have shown great interest among the scientific community. However, the limited knowledge about the charge carrier transport mechanisms and lattice thermal conductivity of the Perovskites significantly affects the device performances, including the lifetime and stability of the sensitizer. This work reports the carrier mobility and lattice thermal conductivity of the orthorhombic $RbMI_3$ (where M=Sn and Ge), using the deformation potential theory and Slack's model, respectively. The mechanical stability has been confirmed for both the structures, and the highest shear anisotropy is observed for $RbSnI_3$. The mobility of the electrons is higher than holes, and the highest mobility is observed along (010) direction for both the structures at low temperatures. Ultra-low-lattice thermal conductivity of 0.237 and 0.402 W/m.K have been observed at the room temperature for $RbSnI_3$ and $RbGeI_3$, respectively, which are consistent with the available experimental values for all inorganic perovskites.

Keywords: Perovskites; Deformation potential theory; Slack's model;

Introduction:

The fantastic efficiency hike of the perovskites from 3.8%[1] in 2009 to 25%[2] in 2021 is due to relatively high absorption coefficients, high charge carrier mobilities, and long diffusion lengths[3-6], making it attractive to the researchers in the photovoltaic group. The engineering of the composition and the effective coating are two main approaches that increase the photo conversion efficiency[7]. The efficiency of the perovskite solar cell (PSC) has been raised[8-11] steeply from 3% to 11% from 2012 to 2014, mostly achieved using mesoporous TiO_2. The increase in efficiency[12-16] is rather slowly and continuously reached 25.2% from 2015 to 2019, mainly achieved by changing the composition. However, thermal stability and toxicity are still the major concerns while the efficiency of PSC is appreciably improved. The thermal stability and heat dissipation can affect the lifetime and performance of the devices. Besides, continuous solar irradiation can induce the device temperature the device temperature above 350 K, further reducing the device stability. Various intrinsic factors, including ion migration, thermal instability, and hygroscopicity, are responsible for the instability of the perovskites. The thermal instability and ion migration have been addressed by tuning the composition[18]. So the decomposition energy can be increased through A site (of ABX_3) doping[19] or replacement[17,20]. The most efficient perovskite solar cell contains toxic Pb. Therefore, the low toxicity/Pb free perovskite solar cell with comparable performance is always preferred. This issue is also being addressed by mixing or replacing Pb with a suitable element[21,22]. Furthermore, the perovskites' mechanical properties can also deliver information about the fundamental properties such as acoustic behaviour and interatomic potentials. Hence, studying the mechanical and transport properties is important to design a better environment-friendly perovskite solar cell.

The structural along with electronic, and optical properties of Pb free orthorhombic $RbMI_3$ (where M=Sn and Ge) were previously studied[23]. The mechanical properties, lattice thermal conductivity, and the charge carrier mobility of $RbSnI_3$ and $RbGeI_3$ are studied and the results are reported in this article. The deformation potential theory within the charge carrier acoustic phonon scattering regime is used to estimate the charge carrier mobility whereas Slack's equation is used for the estimation

https://doi.org/10.36375/prepare_u.iiche.a383

of the lattice thermal conductivity. These methods are computationally less expensive compared to the costly phonon calculations.

Computational methods:

All the first principle based calculations are estimated within the full-potential linearized augmented plane wave (FP-LAPW) method using WIEN2k[24]. The mechanical properties and the deformation potentials of $RbMI_3$ are estimated using PBE[25] exchange correlation functional excluding the spin orbit coupling effect. RKmax of 9 and 8 are set for $RbSnI_3$ and $RbGeI_3$, respectively, while Kmesh of 9×20×5 and 6×13×3 are used. Three different types of strains [a) Orthorhombic volume changing strains of ±1%, ±2%, +3%; b) monoclinic volume conserving strains of ±1%, ±2%, +3% and c) orthorhombic volume conserved strains of ±1%, ±2%, ±3%, +4%] are applied to the relaxed structures to estimate elastic coefficients[26]. The elastic moduli for a polycrystalline sample are measured using Voigt (V) approximation corresponding to the upper limit and of the actual elastic moduli and Reuss (R) approximation corresponding to the lower limit. The bulk (B_V and B_R) and shear modulus (G_V and G_R) in Voigt and Reuss approximations are estimated as[27,28]:

$$\boldsymbol{B_V = \left(\frac{1}{9}\right)[C_{11} + C_{22} + C_{33} + 2(C_{12} + C_{13} + C_{23})]},$$

$$\boldsymbol{B_R = \frac{1}{(S_{11}+S_{22}+S_{33})+2(S_{12}+S_{13}+S_{23})}},$$

$$\boldsymbol{G_V = \frac{1}{15}(C_{11} + C_{22} + C_{33} - C_{12} - C_{13} - C_{23}) + \frac{1}{5}(C_{44} + C_{55} + C_{66})},$$

$$\boldsymbol{G_R = \frac{15}{4(S_{11}+S_{22}+S_{33})-4(S_{12}+S_{13}+S_{23})+3(S_{44}+S_{55}+S_{66})}}.$$

where, $\boldsymbol{S_{ij}}$ are the elastic compliance constants.
Later, Hill approximation provide the bulk modulus (B) and shear modulus (G) as follows[29]:

$$\boldsymbol{B = \frac{B_V+B_R}{2}},$$
$$\boldsymbol{G = \frac{G_V+G_R}{2}}.$$

The Young's modulus and Poisson's ratio are estimated using bulk and shear modulus obtained from Hill approximation as following:

$$\boldsymbol{E = \frac{9BG}{3B+G}};$$
$$\boldsymbol{\sigma = \frac{3B - 2G}{2(3B + G)}}.$$

The directional dependence of Young's modulus and Bulk modulus are estimated using the following formulae[30]:

$$\boldsymbol{E^{-1} = S_{11}l_1^4 + S_{22}l_2^4 + 2S_{13}l_1^2l_3^2 + 2S_{23}l_2^2l_3^2 + S_{55}l_1^2l_3^2 + S_{44}l_2^2l_3^2 + S_{33}l_3^4 + 2S_{12}l_1^2l_2^2 + S_{66}l_1^2l_2^3},$$
$$\boldsymbol{B^{-1} = (S_{11} + S_{12} + S_{13})l_1^2 + (S_{12} + S_{22} + S_{23})l_2^2 + (S_{13} + S_{23} + S_{33})l_3^2}.$$

The mobility of charge carriers is estimated with the deformation potential theory[31] by fitting the CBM (conduction band minimum) and VBM (valence band maximum) to strains of (0%, ±0.5% and ±1%) along three different directions ((100), (010) and (001)) using:

$$\mu_{ij} = \frac{(8\pi)^{1/2}\hbar^4 e C_{ij}}{3{m_{eff}}^{5/2}(K_B T)^{3/2}{D_p}^2},$$

where, C_{ij}, D_p and T are elastic coefficients, effective mass, deformation potential and temperature, respectively. 1s core state of the halogen (I) is used as the reference level to align all eigenvalues for both $RbSnI_3$ and $RbGeI_3$.

Results and Observations:

Mechanical Properties:

The different elastic coefficients are estimated for the orthorhombic structures of $RbMI_3$ and are listed in Table I. The conditions for an orthorhombic structure to be mechanically stable are[32]:

$$C_{11} > 0;$$
$$C_{22} > 0;$$
$$C_{33} > 0;$$
$$C_{44} > 0;$$
$$C_{55} > 0;$$
$$C_{66} > 0;$$
$$(C_{11} + C_{22} - 2C_{12}) > 0:$$
$$(C_{11} + C_{33} - 2C_{13}) > 0:$$
$$(C_{22} + C_{33} - 2C_{23}) > 0:$$
$$(C_{11} + C_{22} + C_{33} + 2C_{12} + 2C_{13} + 2C_{23}) > 0.$$

Both the structures $RbSnI_3$ and $RbGeI_3$ show the mechanical stability. The deformation resistances are found to be stronger along the axial one compared to the non-axial cases. The stronger bonding is observed along the (001) direction for both $RbMI_3$ whereas $RbGeI_3$ show the strongest bonding. TABLE II show values of elastic moduli and anisotropy for $RbSnI_3$ and $RbGeI_3$. The larger values of elastic moduli of $RbGeI_3$ suggest the stronger directional bonding of atoms. The interatomic forces between atoms in both the structures are central in nature as the Poisson's ratio lie within the range of 0.25 and 0.50. $RbGeI_3$ also

https://doi.org/10.36375/prepare_u.iiche.a383

exhibits the higher stability against shear due its lower Poisson's ratio value of 0.313. Moreover, the smaller $\frac{G}{B}$ values (< 0.57) 3 of both $RbMI_3$ confirm their ductility behaviour. Another important mechanical property is

TABLE I: Elastic coefficients in Gpa for $RbMI_3$.

M	C_{11}	C_{22}	C_{33}	C_{12}	C_{13}	C_{23}	C_{44}	C_{55}	C_{66}
Sn	20.087	30.032	35.089	15.431	12.750	9.420	6.392	5.354	8.857
Ge	28.209	31.901	39.182	16.684	14.712	9.684	6.849	7.991	10.141

the elastic anisotropy and it can induce micro cracks in the material. Shear anisotropy[13] in {100}, {010} and {001} planes (A_{100}, A_{001} and A_{001}) and the universal anisotropy[14] (A^U) are estimated using:

$$A_{100} = \frac{4C_{44}}{C_{11}+C_{33}-2C_{13}};$$
$$A_{010} = \frac{4C_{55}}{C_{22}+C_{33}-2C_{23}};$$
$$A_{001} = \frac{4C_{66}}{C_{11}+C_{22}-2C_{12}};$$
$$A^U = 5\frac{G_V}{G_R} + \frac{B_V}{B_R} - 6.$$

The deviation of shear anisotropy values from 1 suggests the existence of anisotropy and the higher shear anisotropy is observed in $RbSnI_3$. The deviation of A^U from 0 for $RbMI_3$ also show the anisotropic nature, which is again larger in RbSnI3. The directional dependence of E (Young's modulus)[35] and B (Bulk Modulus) also suggest the existence of anisotropy for both the structures as shown in the FIG. 1 and FIG. 2 respectively, where the deviation from the sphere confirms the anisotropy. Both FIG. 1 and FIG. 2 also shows the larger anisotropy for $RbSnI_3$.

TABLE II: Elastic moduli in GPa and anisotropy for $RbMI_3$.

M	E	B	G	σ	G/B	A_{100}	A_{01}	A_{00}	A^U
Sn	18.020	17.560	6.780	0.328	0.386	0.862	0.463	1.840	0.848
Ge	22.450	20.111	8.543	0.313	0.425	0.722	0.616	1.517	0.416

FIG. 1: The directional dependence of Young's modulus E for $RbSnI_3$ (left) and $RbGeI_3$ (right), respectively.

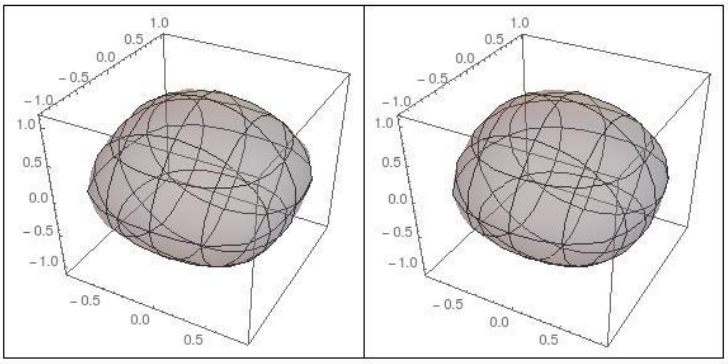

FIG. 2: The directional dependence of Bulk modulus B for both $RbSnI_3$ (left) and $RbGeI_3$ (right).

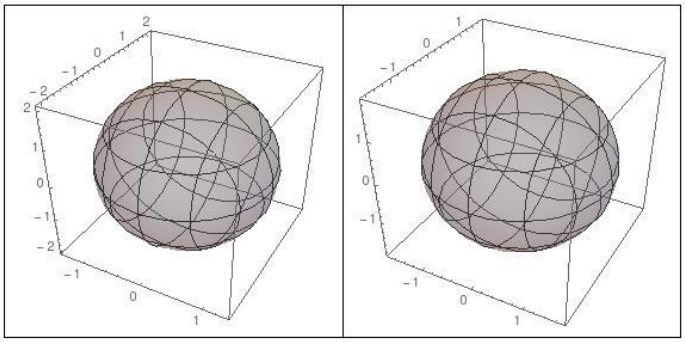

The charge carrier mobility and lattice thermal conductivity:

The deformation potential theory is considered to estimate the charge carrier mobilities for the carrier acoustic phonon scattering regime. The other scatterings due to optical phonons, impurities and defects could also be important but the scattering due to the carrier acoustic phonon is believed to be appropriate at the low temperature (100 K) where, the orthorhombic structures $RbMI_3$ are stable. Hence, the deformation potentials D_p required to estimate the mobility for both the structures are calculated and listed in TABLE III. The estimated charge carrier mobilities μ_{ij} at 100 K are also enlisted in TABLE IV whereas the required effective masses of carriers are considered from the previous report[23]. The TABLE IV shows the mobility of electrons are higher than that of holes along all three directions for both the structures. The higher electron mobility is observed along (010)

https://doi.org/10.36375/prepare_u.iiche.a383

direction for both whereas $RbSnI_3$ shows the highest one. The smaller effective masses for electrons plays

TABLE III: Deformation potential D_p in eV for $RbMI_3$.

M	Along (100)		Along (010)		Along (001)	
	Electron	Hole	Electron	Hole	Electron	Hole
Sn	-12.991	-16.848	-16.805	-14.308	-12.991	-15.843
Ge	-14.341	-16.077	-19.459	-17.280	-13.057	-15.307

significant role here in determining the mobility due to the insignificant differences in D_p and μ_{ij}.

TABLE IV: Mobility μ_{ij} in cm^2/Vs at 100 K for $RbMI_3$.

M	Along (100)		Along (010)		Along (001)	
	Electron	Hole	Electron	Hole	Electron	Hole
Sn	127.911	1.258	77369.719	312.626	2.714	0.891
Ge	235.361	1.929	35482.601	267.558	7.417	1.165

Slack's equation[36] is an inexpensive way to find the lattice thermal conductivity (K_l) compared to the ethod using phonon DOS and also provide a rough estimate of l. This equation requires information about the anharmonicity (Gruinsen parameter ϒ) of the system and the Debye temperature (Θ_D), which are obtained from the elastic moduli. Slack's equation uses:

$$K_l = \frac{AM_a\delta\Theta_D^3}{\Upsilon Tn^{2/3}};\ A = \frac{2.43\times10^{-8}}{1-\frac{0.514}{\Upsilon}+\frac{0.228}{\Upsilon^2}};\ \Upsilon = \frac{9\left(v_l^2-\frac{4}{3}v_t^2\right)}{2\left(v_l^2+2v_t^2\right)};$$

where, M_a, δ, v_t, v_t and T are the average atomic mass, the volume per atom, the longitudinal and transverse acoustic velocity and temperature, respectively.

All the required values along with K_l estimated at 300 K are shown in TABLE V. The lower lattice thermal conductivity of 0.237 for $RbSnI_3$ and 0.402 W/m/K are observed for $RbGeI_3$, this agrees well with the reported low lattice thermal conductivity found for all inorganic perovskites[37].

TABLE V: Lattice thermal conductivity K_l in W/m/K at 300 K for $RbSnI_3$ and $RbGeI_3$.

$RbMI_3$	M_a	δ	n	v_t	v_{l1}	Θ_D	K_l
$RbSnI_3$	116.97	3.532	20	1240.53	2457.15	117.21	0.237
$RbGeI_3$	107.76	3.439	20	1394.22	2677.28	135.01	0.402

Conclusions:

The mechanical property, the lattice thermal conductivity and the mobility are studied for both orthorhombic $RbSnI_3$ and $RbGeI_3$. The highest bonding is observed for $RbGeI_3$ along (001) and $RbSnI_3$ shows the highest anisotropy while both the structures show the mechanical stability. $RbSnI_3$ exhibits the higher electron mobility along (010) direction whereas $RbGeI_3$ displays the higher lattice thermal conductivity. The values of the charge carrier mobility are highly dependent on the carrier's effective masses. The lower thermal conductivity and the higher effective masses are observed in $RbMI_3$, makes them perfect material for thermoelectric applications[37].

References:

(1) A. Kojima, K. Teshima, Y. Shirai, and T. Miyasaka, Organometal halide perovskites as visible light sensitizers for photovoltaic cells, Journal of the American Chemical Society 131, 6050 (2009).
(2) N. R. E. L. (NREL), Best research-cell efficiencies, https://www.nrel.gov/pv/assets/pdfs/best-research-cell-efficiencies.20191106.pdf (2020).
(3) W. S. Yang, B.-W. Park, E. H. Jung, N. J. Jeon, Y. C. Kim, D. U. Lee, S. S. Shin, J. Seo, E. K. Kim, J. H. Noh, et al., Iodide management in formamidinium-lead-halide{based perovskite layers for efficient solar cells, Science 356, 1376 (2017).
(4) W. A. Dunlap-Shohl, Y. Zhou, N. P. Padture, and D. B. Mitzi, Synthetic approaches for halide perovskite thin films, Chemical reviews 119, 3193 (2018).
(5) X. Meng, X. Cui, M. Rager, S. Zhang, Z. Wang, J. Yu, Y. W. Harn, Z. Kang, B. K. Wagner, Y. Liu, et al., Cascade charge transfer enabled by incorporating edge-enriched graphene nanoribbons for mesostructured perovskite solar cells with enhanced performance, Nano Energy 52, 123 (2018).
(6) H. Dong, J. Xi, L. Zuo, J. Li, Y. Yang, D. Wang, Y. Yu, L. Ma, C. Ran, W. Gao, et al., Conjugated molecules \bridge": Functional ligand toward highly efficient and long-term stable perovskite solar cell, Advanced Functional Materials 29, 1808119 (2019).

(7) J. Y. Kim, J.-W. Lee, H. S. Jung, H. Shin, and N.-G. Park, High-efficiency perovskite solar cells, Chemical Reviews 120, 7867 (2020).
(8) H.-S. Kim, C.-R. Lee, J.-H. Im, K.-B. Lee, T. Moehl, A. Marchioro, S.-J. Moon, R. Humphry-Baker, J.-H. Yum, J. E. Moser, et al., Lead iodide perovskite sensitized all-solid-state submicron thin film mesoscopic solar cell with efficiency exceeding 9%, Scientific reports 2, 1
(2012).
(9) O. H. Perovskites, Efficient hybrid solar cells based on meso-superstructured, Phys. Rev. Lett 92, 210403 (2004).
(10) J.-H. Im, C.-R. Lee, J.-W. Lee, S.-W. Park, and N.-G. Park, 6.5% efficient perovskite quantum dot-sensitized solar cell, Nanoscale 3, 4088 (2011).
(11) J. H. Heo, S. H. Im, J. H. Noh, T. N. Mandal, C.-S. Lim, J. A. Chang, Y. H. Lee, H.-j. Kim, A. Sarkar, M. K. Nazeeruddin, et al., Efficient inorganic{organic hybrid heterojunction solar cells containing perovskite compound and polymeric hole conductors, Nature photonics 7, 486 (2013).
(12) M. A. Green, Y. Hishikawa, E. D. Dunlop, D. H. Levi, J. Hohl-Ebinger, and A. W. Ho-Baillie, Solar cell efficiency tables (version 52), Progress in Photovoltaics: Research and Applications 26, 427 (2018).
(13) M. A. Green, E. D. Dunlop, J. Hohl-Ebinger, M. Yoshita, N. Kopidakis, and X. Hao, Solar cell efficiency tables (version 58), Progress in Photovoltaics: Research and Applications 29, 657 (2021).
(14) J. Burschka, N. Pellet, S.-J. Moon, R. Humphry-Baker, P. Gao, M. K. Nazeeruddin, and M. Gr•atzel, Sequential deposition as a route to high-performance perovskite-sensitized solar cells, Nature 499, 316 (2013).
(15) N. Ahn, D.-Y. Son, I.-H. Jang, S. M. Kang, M. Choi, and N.-G. Park, Highly reproducible perovskite solar cells with average efficiency of 18.3% and best efficiency of 19.7% fabricated via lewis base adduct of lead (ii) iodide, Journal of the American Chemical Society 137, 8696
(2015).
(16) D.-Y. Son, J.-W. Lee, Y. J. Choi, I.-H. Jang, S. Lee, P. J. Yoo, H. Shin, N. Ahn, M. Choi, D. Kim, et al., Self-formed grain boundary healing layer for highly efficient CH3NH3PbI3 perovskite solar cells, Nature Energy 1, 1 (2016).
(17) P. Wang, X. Zhang, Y. Zhou, Q. Jiang, Q. Ye, Z. Chu, X. Li, X. Yang, Z. Yin, and J. You, Solvent-controlled growth of inorganic perovskite fillms in dry environment for efficient and stable solar cells, Nature communications 9, 1 (2018).
(18) N. Arora, M. I. Dar, A. Hinderhofer, N. Pellet, F. Schreiber, S. M. Zakeeruddin, and M. Gr•atzel, Perovskite solar cells with cuscn hole extraction layers yield stabilized efficiencies greater than 20%, Science 358, 768 (2017).
(19) M. Saliba, T. Matsui, K. Domanski, J.-Y. Seo, A. Ummadisingu, S. M. Zakeeruddin, J.-P. Correa-Baena, W. R. Tress, A. Abate, A. Hagfeldt, et al., Incorporation of rubidium cations into perovskite solar cells improves photovoltaic performance, Science 354, 206 (2016).
(20) W. Zhou, Y. Zhao, X. Zhou, R. Fu, Q. Li, Y. Zhao, K. Liu, D. Yu, and Q. Zhao, Light independent ionic transport in inorganic perovskite and ultrastable Cs-based perovskite solar cells, The journal of physical chemistry letters 8, 4122 (2017).
(21) W. Ke, C. C. Stoumpos, and M. G. Kanatzidis, \unleaded" perovskites: status quo and future prospects of tin-based perovskite solar cells, Advanced Materials 31, 1803230 (2019).
(22) F. Giustino and H. J. Snaith, Toward lead-free perovskite solar cells, ACS Energy Letters 1, 1233 (2016).
(23) A. Nyayban, S. Panda, and A. Chowdhury, Structural, electronic and optical properties of lead free rb based triiodide for photovoltaic application: an ab initio study, 33, 375702 (2021).
(24) P. Blaha, K. Schwarz, G. K. Madsen, D. Kvasnicka, J. Luitz, et al., wien2k, An augmented plane wave+ local orbitals program for calculating crystal properties (2001).
(25) J. P. Perdew, K. Burke, and M. Ernzerhof, Generalized gradient approximation made simple, Physical review letters 77, 3865 (1996).
(26) M. Jamal, M. Bilal, I. Ahmad, and S. Jalali-Asadabadi, Irelast package, Journal of Alloys and Compounds 735, 569 (2018).
(27) W. Voigt, Lehrbuch der kristallphysik (teubner, stuttgart, 1928).
(28) A. Reu_, Berechnung der ie_grenze von mischkristallen auf grund der plastizit•atsbedingung f•ur einkristalle., ZAMM-Journal of Applied Mathematics and Mechanics/Zeitschrift f•ur Angewandte Mathematik und Mechanik 9, 49 (1929).
(29) R. Hill, The elastic behaviour of a crystalline aggregate, Proceedings of the Physical Society. Section A 65, 349 (1952).
(30) Q. Wei, M. Zhang, L. Guo, H. Yan, X. Zhu, Z. Lin, and P. Guo, Ab initio studies of novel carbon nitride phase c2n2 (ch2), Chemical Physics 415, 36 (2013).
(31) J. Bardeen and W. Shockley, Deformation potentials and mobilities in non-polar crystals, Physical review 80, 72 (1950).
(32) G. Sin'Ko and N. Smirnov, Ab initio calculations of elastic constants and thermodynamic properties of bcc, fcc, and hcp al crystals under pressure, Journal of Physics: Condensed Matter 14, 6989 (2002).
(33) P. Ravindran, L. Fast, P. A. Korzhavyi, B. Johansson, J. Wills, and O. Eriksson, Density functional theory for calculation of elastic properties

of orthorhombic crystals: Application to tisi 2, Journal of Applied Physics 84, 4891 (1998).
(34) C. M. Kube, Elastic anisotropy of crystals, AIP Advances 6, 095209 (2016).
((35) O. Gomis, R. Vilaplana, F. J. Manj_on, D. Santamaria-Perez, D. Errandonea, E. Perez, Gonzalez, J. L_opez-Solano, P. Rodr__guez-Hern_andez, A. Mu~noz, I. Tiginyanu, et al., Highpressure study of the structural and elastic properties of defect-chalcopyrite hgga2se4, Journal of Applied Physics 113, 073510 (2013).
(36) G. A. Slack, Nonmetallic crystals with high thermal conductivity, Journal of Physics and Chemistry of Solids 34, 321 (1973).
(37) W. Lee, H. Li, A. B.Wong, D. Zhang, M. Lai, Y. Yu, Q. Kong, E. Lin, J. J. Urban, J. C. Grossman, et al., Ultralow thermal conductivity in all-inorganic halide perovskites, Proceedings of the National Academy of Sciences 114, 8693 (2017).